■ JSME Medal for Outstanding Paper in 2004 ■

Subsurface Crack Initiation and Propagation Mechanism under the Super-Long Fatigue Regime for High Speed Tool Steel (JIS SKH51) by Fracture Surface Topographic Analysis*

Kazuaki SHIOZAWA**, Yuuichi MORII*** and Seiichi NISHINO**

In order to study the subsurface crack initiation and propagation mechanism of high strength steel under a very high cycle fatigue regime, computational simulation with fracture surface topographic analysis (FRASTA) was carried out for subsurface fatigue crack initiated specimens of high speed tool steel (JIS SKH51) obtained from the rotating bending fatigue test in air. A remarkable area formed around the nonmetallic inclusion inside the fish-eye region on the fracture surface, which is a feature on the fracture surface in super long fatigue. This so-called GBF (granular-bright-facet) was observed in detail by a scanning probe microscope and a three-dimensional SEM. The GBF area, in which a rich carbide distribution was detected by EPMA, revealed a very rough and granular morphology in comparison with the area inside the fish-eye. It was clearly simulated by FRASTA that multiple microcracks were initiated and dispersed by the decohesion of a spherical carbide from the matrix around a nonmetallic inclusion, and converged into the GBF area during the fatigue process. After the formation of the GBF area, interior cracks grew radially and a fish-eye pattern formed on the fracture surface.

Key Words: Long Life Fatigue, Subsurface Crack, Crack Initiation Mechanism, Fractography, Topographic Analysis, High Speed Tool Steel

1. Introduction

A number of researchers[1]-[16] have reported a remarkable shape of the $S-N$ curve from the experimental results obtained from fatigue tests using specimens of some high-strength steel and case-hardened steel. The fatigue failures occurred at small internal defects in the subsurface zone of a material at low stress amplitude levels which were below the conventional fatigue limits, and in a high-cycle region of more than 10^7 cycles, i.e. ultra-long life. Normally, surface fatigue crack initiation occurs at high-stress amplitude and low cycles. There is a definite stress range where the crack initiation site changes from the surface to a subsurface defect, giving a step-wise $S-N$ curve; i.e. there are two knees on the curve. The other $S-N$ curve named as a duplex $S-N$ curve, different from the step-wise $S-N$ curve, was obtained from the rotary-bending fatigue tests using a specimen of a high-carbon-chromium bearing steel, JIS SUJ2[2],[4],[8]-[11]. The latter consists of two different $S-N$ curves corresponding to the respective fracture mode: One of the two $S-N$ curves appears at a high-stress amplitude level and low number of cycles, and is governed by a surface fracture mode as a result of the surface crack initiation and growth. The other $S-N$ curve appears at a high number of cycles and is governed by internal crack initiation and growth. The internal fracture mode is governed by a non-metallic inclusion, and is distributed over a wide range of stress amplitudes, which are not only below a conventional fatigue limit defined as the threshold for the surface fracture mode, but also above the fatigue limit. It is very important for the establishment of a reliable and safe fatigue design for mechanical elements to clarify the mechanism of internal fatigue fracture occurring below a conventional fatigue limit.

* Received 28th September, 2005 (No. 03-0669). Japanese Original: Trans. Jpn. Soc. Mech. Eng., Vol.70, No.691, A (2004), pp.495–503 (Received 4th June, 2004)

** Department of Mechanical and Intellectual Systems Engineering, University of Toyama, 3190 Gofuku, Toyama 930–8555, Japan.
E-mail: shiozawa@eng.toyama-u.ac.jp

*** Komatsu Ltd., Awazu Plant, Tsu 23 Futsu-machi, Komatsu 923–0392, Japan

In a series of studies on ultra-long life fatigue behavior in a high-carbon-chromium bearing steel, JIS SUJ2[2),(4),(15),(16)], and a high speed tool steel, JIS SKH51[17),(18)], a distinctive feature was observed in the vicinity of a non-metallic inclusion at the fracture origin inside the fish-eye on fracture surfaces resulting from subsurface crack initiation and propagation in a high-cycle fatigue regime. A white-bright facet area was found at the fracture origin by SEM observation and this area revealed a very rough and granular morphology in comparison with the area inside the fish-eye. Authors have named this a 'granular-bright-facet' (GBF) in previous papers[2),(4),(15)-(18)]. Additionally, it was also verified experimentally that the size of the GBF is the same as the optically dark area (ODA) named by Murakami et al.[3),(7),(12),(13)] It was indicated that the formation of the GBF area during the long fatigue process controls the internal fracture mode, and is an important factor clarifying fatigue behavior in a very high cycle regime and ensuring the long durability of machine elements and structures.

The remarkable area formed around the nonmetallic inclusion inside the fish-eye region on the fracture surface was given various names, such as fine granular area (FGA)[1),(9)-(11)] and rough surface area (RSA)[14)]. The formation mechanism of the GBF area has yet to be elucidated, because it is difficult to directly observe the behavior of subsurface crack initiation and propagation. The authors have proposed the mechanism of GBF formation in a very high cycle fatigue regime as a 'dispersive decohesion of spherical carbide' model, based on the experimental results of detailed observations of fracture surface using specimens of high-carbon-chromium bearing steel, JIS SUJ2, of which the carbon content is 1.01%w/w[19),(20)].

The aim of this study is to clarify the mechanism of the formation of a GBF area in the vicinity of an inclusion, and to verify the adequacy for the model of dispersive decohesion of spherical carbide. The specimen used in this study is a high-speed tool steel, JIS SKH51, of which carbon content is 0.63%w/w, and lower than that of JIS SUJ2. Detailed observations of the morphology in a GBF area of the specimen obtained from a cantilever type rotary bending fatigue in air were carried out using a three-dimensional SEM and a scanning probe microscope (SPM). The fracture surface topographic analysis (FRASTA) method proposed by Kobayashi and Shockey[21)] was applied to simulate the fatigue fracture process.

2. Experimental Procedures

2.1 Testing materials and specimens

The material used in this study was a high speed tool steel, JIS SKH51. The chemical composition (mass percentage) of this steel is: 0.63 C, 5.24 Mo, 6.02 W and 2.1 V. Hourglass-shaped specimens with a minimum diameter of 3 mm and round notch radius of 7 mm were machined. The specimens were heated in a vacuum at 1 453 K, and oil-cooled at 823 K twice, tempered in a vacuum at 823 K and subsequently air-cooled. The round notch surface was polished by a grinder with a mesh of #100. The elastic stress concentration factor of the specimen was 1.06. The average Vickers hardness of the heat-treated material was HV798 and was uniform from the specimen surface to the inside.

Figure 1 shows the microstructure of the heat-treated materials observed by SEM, which was prepared with micro-etching by Nital (a) and electro-etching (b). It can be assessed from the photographs that many carbide particles are distributed in the matrix, which is a tempered martensitic structure consisting of an average prior-austenitic grain size of 6.1 μm. From Fig. 1 (b), particles of various shapes and sizes were noted in the matrix. These features were best identified using back scattered electron imaging, appearing as the white or dark particles in Fig. 2 (b), as compared to the secondary electron image in Fig. 2 (a). Large precipitated particles, indicated as 'a' in the photograph, appeared as white, and were carbide particles with combined molybdenum, vanadium and tungsten by the measurement with EPMA. Fine and sphere-like particles randomly distributed with in the matrix are observed in Fig. 2. Some particles appear as white in the back scattered electron image, indicated as 'b', and were chromium carbides. The other particles appear as dark

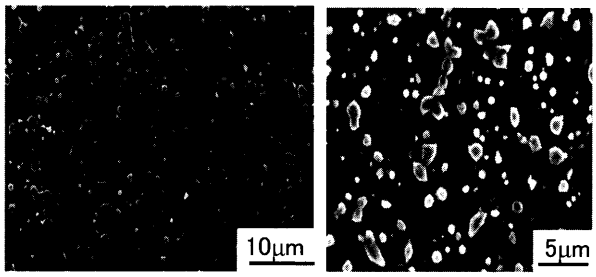

(a) Etched by Nital (b) Electro-polished

Fig. 1 Microstructure of high speed tool steel, JIS SKH51, observed by SEM

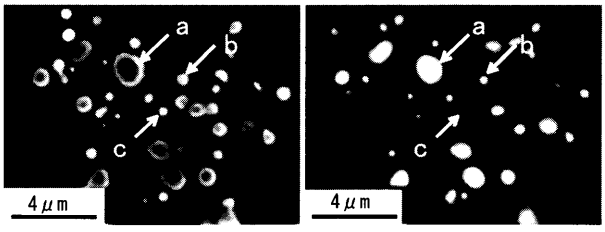

(a) Secondary electron image (b) Back scattered electron image

Fig. 2 Secondary electron image (a) and backscattered electron image (b) of carbide particles within the JIS SKH51 matrix

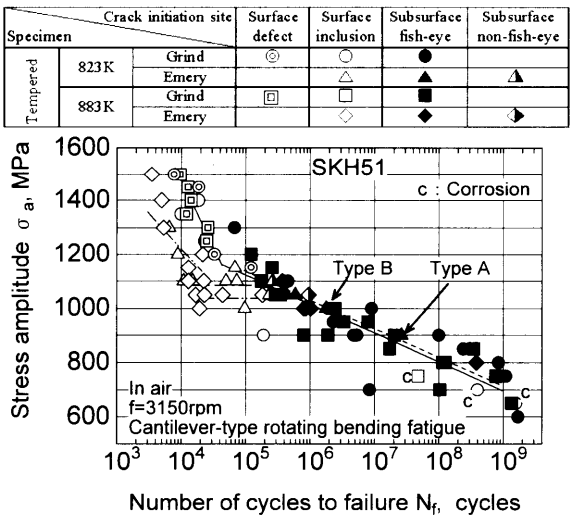

Fig. 3 The $S-N$ curves of high-speed tool steel, JIS SKH51 obtained from the cantilever-type rotary bending fatigue tests[17),(18)]

shapes, indicated as 'c', and were iron carbide (cementite, Fe_3C).

2.2 Characteristics of an $S-N$ curve

The $S-N$ curve obtained from the fatigue tests using the grinder polished specimens (referred to as grind) is shown in Fig. 3[17),(18)]. Fatigue tests were performed in an open environment at room temperature using a four-axis cantilever-type rotary bending fatigue machine, which was operated at 3 150 rpm ($f=52.5$ Hz)[9]. In this figure, some experimental results obtained from the specimens polished by emery-paper (referred to as emery) and tempered at 883 K are also shown. Fatigue fracture in all four types of specimen is governed by a surface fracture mode as a result of the surface crack initiation and growth at a high-stress amplitude level and low number of cycles. The surface crack initiation site is a surface defect and surface inclusion, depending on the condition of surface finish. On the other hand, the internal fracture mode appears at a high number of cycles and a low-stress amplitude level, and is governed by a non-metallic inclusion. It can be seen from the $S-N$ curve obtained from the emery-polished specimens that there is a definite stress range where the crack initiation site changes from a surface to a subsurface defect, giving a step-wise $S-N$ curve (the two knees on the curve). A step-wise $S-N$ curve was not clear for the specimens surface-polished by a grinder, because of the compressive residual stress on the surface layer formed by the grinding. The effects of the surface-finishing and tempering temperature on the $S-N$ curve governed by internal fracture mode cannot be observed in Fig. 3.

From SEM observations, distinctive features of the fracture surface, GBF, were observed near a non-metallic inclusion at the fracture origin inside the fish-eye zone for specimens ruptured at the high-cycles of a life time

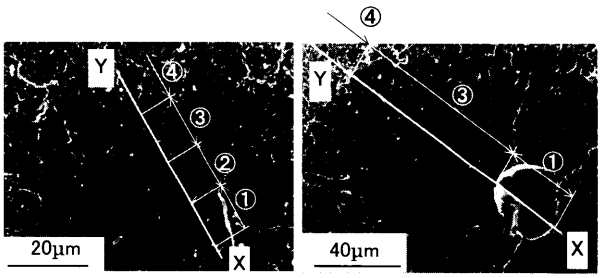

(a) Type A ($\sigma_a=900$ MPa, $N_f=2.5\times10^7$)

(b) Type B ($\sigma_a=1\,000$ MPa, $N_f=1.9\times10^6$)

Fig. 4 SEM micrographs of a fish-eye on the fracture surface

of over 10^6 cycles and below a stress-amplitude level of 1 000 MPa. Figure 4 shows a typical SEM observation of the fracture surface of an emery-polished specimen tempered at 823 K ruptured at a high number of cycles (indicated as Type A in Fig. 3, $\sigma_a=900$ MPa, $N_f=2.5\times10^7$), and the specimen ruptured after a short fatigue life (indicated as Type B in Fig. 3, $\sigma_a=1\,000$ MPa, $N_f=1.9\times10^6$). A white-bright area, the GBF area, was found in the vicinity of the non-metallic inclusion at the fracture origin of the Type A specimen as shown in Fig. 4 (a). The inclusion was analyzed as a vanadium carbide (VC) by EPMA. On the other hand, a white-bright area (GBF area) was not found in the vicinity of the non-metallic inclusion, which was analyzed as an aluminum oxide (Al_2O_3), in the Type B specimen as shown in Fig. 4 (b).

2.3 FRASTA method

The fracture surface topographic analysis (FRASTA) method is a procedure for computationally reconstructing the process of crack extension in microscopic detail by comparing topographic features of a conjugate area of opposing fracture surfaces[21]. This technique is useful to examine subsurface crack-growth behavior, because it is difficult to directly observe cracks inside a specimen. In this study, the FRASTA method was applied to discuss the formation mechanism of the GBF area.

Precise topographic maps of the fracture surfaces were obtained by a three-dimensional SEM (Hitachi RD-500), and topographic data digitized and stored. The difference in elevation between the highest and the lowest point within the observation field, 6.2 μm for the Type A specimen and 3.8 μm for the Type B specimen, was determined by dividing a 256-gradation sequence. The elevation data in the analytical field, 36 μm×27 μm for the Type A specimen (Fig. 8 (a)) and 54 μm×40 μm for the Type B specimen (Fig. 9 (a)), were characterized in a grid containing 640×480 pixels. In preparation for reconstructing the fracture process, the topographic map of one fracture surface was inverted and superimposed on the map of the conjugate surface. The two maps were then translated and rotated with respect to each other until identifiable corre-

sponding points on the two surfaces were in alignment. The relative distance between the maps was adjusted so that the topographic surfaces overlapped everywhere, i.e. with no spaces between them, and the ruptured specimen was returned to its state before the tests.

The fracture process was reconstructed by increasing the distance between the conjugate maps in small increments. After each displacement the projected area was scanned to determine whether the overlap was still complete or if non-overlapping regions appeared. Gaps between the conjugate maps signified material separation. Gap location and size indicated the location and size of a microcrack. These results can be displayed in two ways; as a series of fracture-area projection plots (FAPPs) or a series of a cross-sectional plots (XSPs). FAPPs display microcrack formation in the fractured plane from the direction perpendicular to the fracture plane. XSPs show sections made perpendicular to the crack front and display how the two surfaces match each other, as well as the amount of overlap.

3. Detailed Observation of Fracture Surface

3.1 Morphology of fracture surface

In order to discuss the morphology of the fish-eye pattern in detail, surface roughness measurements of the fracture surface along a cutting plane line, XY, shown in Fig. 4 were taken via three-dimensional SEM analysis. The surface roughness curve and values of the surface roughness on each area of fracture surface in the Type A and Type B specimen are shown in Fig. 5 and Table 1. A GBF area in the Type A specimen (indicated as (2) in Fig. 5 (a)) reveals a rough morphology compared with the area inside the fish-eye ((3) in Fig. 5 (a)). The roughness of the GBF area is about 3 times greater than that outside the GBF area. On the other hand, it can be observed in Fig. 5 (b) that a rough morphology does not appear around an inclusion in the Type B specimen.

A definition of an average distance of roughness, S, is given in the margin of Table 1. The S of the GBF area shown in Table 1 is 1.20 μm, which is smaller than that outside the GBF in the fish-eye and outside the fish-eye. This value corresponds to the average diameter of carbide distributed in the matrix, which is 1.13 μm measured by SPM as mentioned below.

3.2 SEM observation of the GBF area

Detail observations of the GBF area in a Type A specimen were made using secondary electron imaging and back scattered electron imaging by SEM. Figure 6 shows

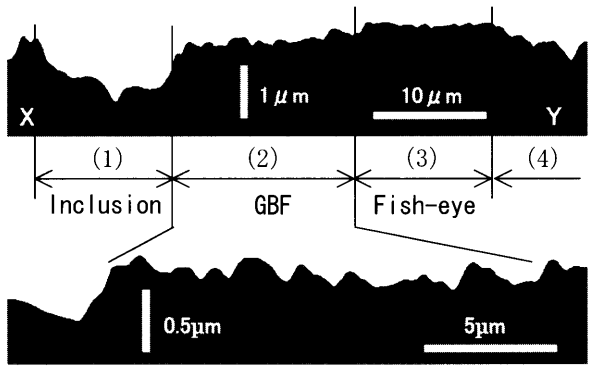

(a) Type A

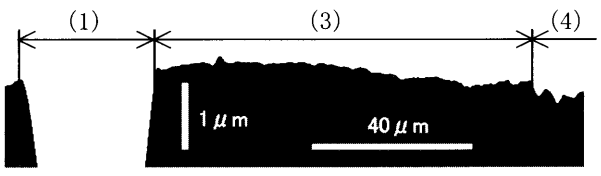

(b) Type B

Fig. 5 Surface roughness plot along a cutting line, XY, on the fracture surface of the Type A and Type B specimen shown in Fig. 4

Table 1 Experimental measurements of surface roughness on the fracture surface

(μm)

Specimen	Roughness	GBF ②	Inside of fish-eye ③	Outside of fish-eye ④
Type A	*Ra*	0.130	0.027	0.227
	Rmax	0.395	0.124	0.937
	*S**	1.204	1.546	1.990
Type B	*Ra*	-	0.028	0.221
	Rmax	-	0.137	1.120
	*S**	-	1.408	1.931

* Definition of "S"

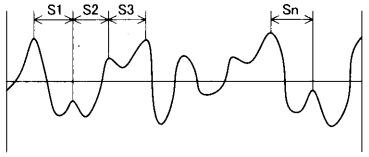

$$S = \frac{1}{n}\sum_i S_i$$

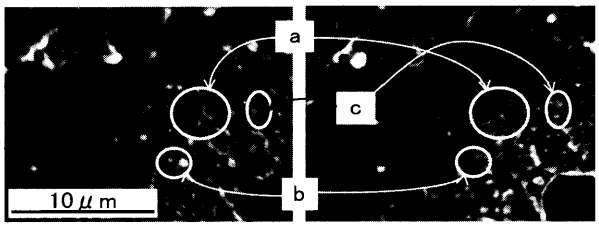

(a) Secondary electron image

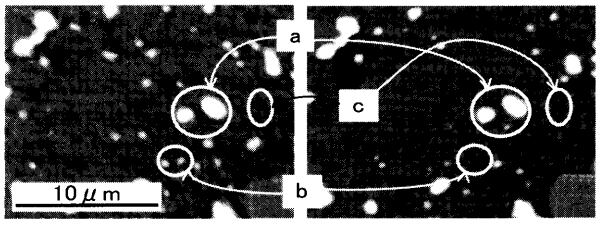

(b) Back scattered electron image

Fig. 6 SEM matching photographs in the GBF area on the fracture surface of the Type A specimen

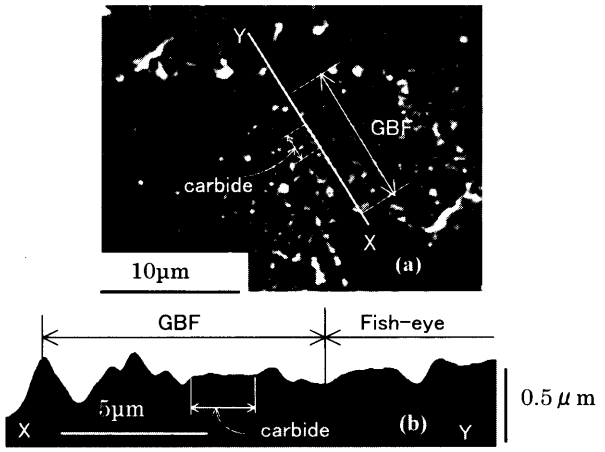

Fig. 7 Surface roughness plot along a cutting line, XY, in the vicinity of Mo-V-W carbide particles on the fracture surface of the Type A specimen

a matching photograph at the GBF area obtained by SEM. The zones enclosed with white-line circles in both photographs correspond to each other at the fracture surface. The letters 'a', 'b' and 'c' in the photographs shows a kind of carbide particle mentioned previously and correspond to Fig. 2. It is understood from Fig. 6 (a) and (b) that a large and gray carbide particle referred to as 'a' on one fracture surface corresponds to a gray particle on the other in the secondary electron image. The particle also shows as a white shape in both back scattered electron images. Therefore, it is suggested that the carbide particle had ruptured during the fatigue process and remains on each fracture surface. For a fine carbide particle referred to as 'b' and 'c', a white (dark) spotty part on one fracture surface corresponds to a dark (white) spotty part on the other in both the secondary electron and back scattered electron image. It is therefore expected from the experimental observations that a white spotty part indicates the remaining carbide particle on one fracture surface, and a dark spotty part indicates the marks of a carbide particle peeled off on the other fracture surface.

Figure 7 shows a surface roughness measurement of the fracture surface along a cutting line crossing the large carbide particle of 'a', XY, shown in Fig. 7 (a). It is seen in Fig. 7 (b) that there is a flat part on the surface roughness plot, corresponding to the carbide particle of 'a' (combined molybdenum, vanadium and tungsten). This is a evidence of a rupture of the carbide particle during the GBF formation.

4. Simulation of Fracture Process by FRASTA Method

4.1 A series of FAPPs

Figures 8 and 9 show a series of fracture-area projection plots (FAPPs) generated by the FRASTA method for a Type A specimen in which the GBF area exists in

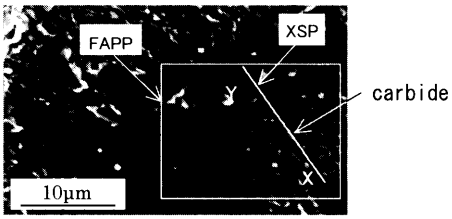

(a) SEM micrograph of analyzed area

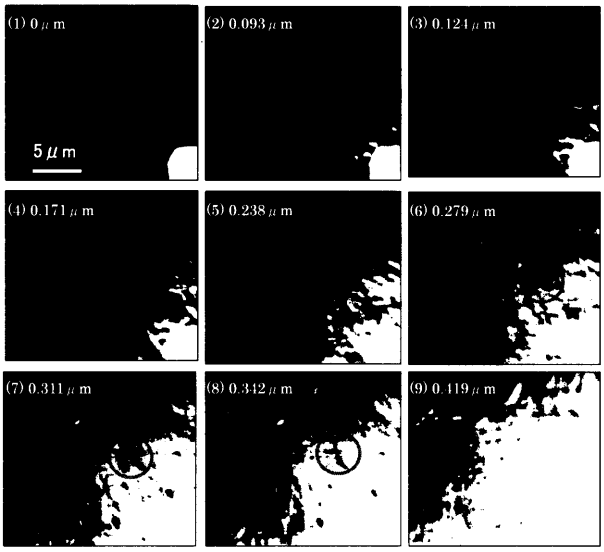

(b) Fracture area projection plots, FAPPs

Fig. 8 Series of fracture-area projection plots (FAPPs) generated by FRASTA for the Type A specimen

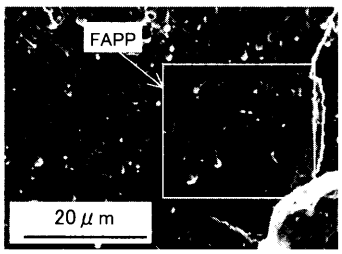

(a) SEM micrograph of analyzed area

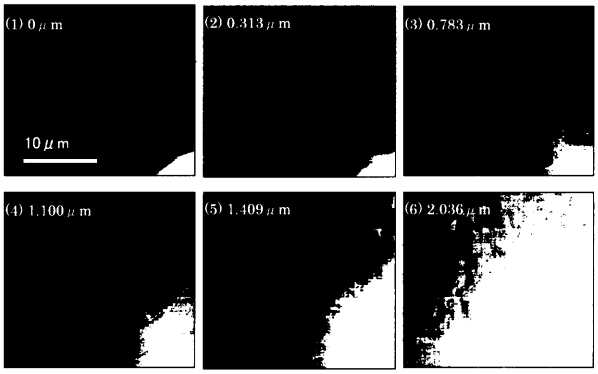

(b) Fracture area projection plots, FAPPs

Fig. 9 Series of fracture-area projection plots (FAPPs) generated by FRASTA for the Type B specimen

the vicinity of an inclusion on the fracture surface, and a Type B specimen in which the GBF area does not exist. The analyzed area enclosed by the white square is shown in (a) of each figure. In these plots, the dark areas indicate the unfractured areas, and the white areas are the fractured ones; showing how these areas change with fracture surface displacement, i.e. fatigue cycling. The number in each plot gives the topographic displacement relative to the reference state. Initially, the conjugate topographic maps were matched by maintaining their reference planes parallel, except for the inclusion which exfoliated out from the fracture surface.

At the stage of a small displacement, i.e. at an early stage of the fatigue process, small spotty white areas can be seen in the vicinity of an inclusion (Fig. 8 (b)). These areas are microcracks initiated during fatigue cycling. As the separation between the conjugate maps increases (this is equivalent to increased fatigue cycles), the multiple microcracks increased in size and number, and then coalesced with each other into the GBF area. After that, the crack grows in a circular shape and forms a fish-eye. On the other hand, the results of FAPPs obtained from the Type B specimen that did not have the GBF area around an inclusion, showed that the fatigue crack was initiated at the inclusion, and increased in size in a circular shape (Fig. 9 (b)).

Fracture behavior of a large carbide particle of combined molybdenum, vanadium and tungsten within a GBF area, was observed in detail on the FAPPs. Areas enclosed by circles in plots of (6) – (8) of Fig. 8 (b) corresponds to the large carbide particle indicated by arrows in Fig. 8 (a). The figure shows that the fracture of the area existing the large carbide particle occurs after the fracture of the surrounding areas.

4.2 A series of XSPs

Figure 10 shows cross-sectional plots, XSPs, of crack growth obtained by displacing topographic contours along the white line XY in Fig. 8 (a), which includes the large carbide particle. The dark-shaded areas are areas where the two topographic surfaces overlap, and indicate that plastic deformation formed at a crack front during crack propagation. In these images, the white area is the fracture area. It can be seen from the XSPs of the Type A specimen that microcracks initiate at a short distance from an inclusion and propagate by increasing the separation. The microcrack coalesces with another one initiated at a different point into a large crack during fatigue cycles. It is confirmed from the XSPs that the large carbide particle delays fracture compared with the surrounding area, i.e. the fracture of the large carbide particle follows that of surrounding area. Therefore, it can be concluded that fatigue crack propagation behavior around a large carbon particle in the GBF area is clearly different from that around a fine carbide particle.

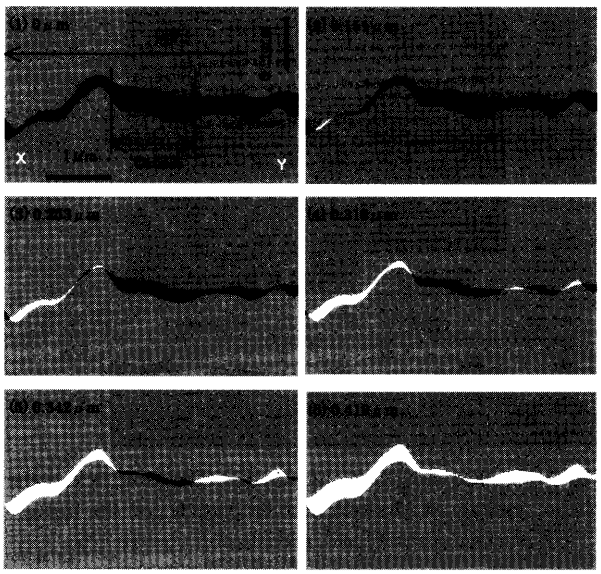

Fig. 10 Analytical results for a series of cross-sectional plots (XSPs) generated by the FRASTA in the region of GBF for the Type A specimen regarding to the rupture of the large carbide

5. Discussion for GBF Formation Mechanism

5.1 SPM observation of GBF area

Detailed observations of the GBF area in a Type A specimen were made at high magnification. Figure 11 (a) shows photograph obtained from the GBF area in the vicinity of the inclusion. There are white and dark spotty parts existing in sequence, resembling the surface of a golf ball. It is noted that the white spotty parts in the GBF area observed on a SEM photograph are due to the halation with spherical carbide particles of low conductivity. Figure 11 (b) and (c) show a precise topographic map of the GBF area obtained by a scanning probe microscope (SPM) observation. It can be seen from the birds-eye pattern shown in Fig. 11 (c) that a granular convex surface is revealed on the GBF area, and corresponds with a white spot on a SEM image in Fig. 11 (a). The arrows correspond to the same part in each photograph.

To discuss the microstructures of the tested materials, SPM observations were carried out using a sample prepared by electro-etching in which the treatment carbides in the material rose to the surface, and a matrix around the carbides was preferentially polished off. Figure 12 shows an example of a SEM and SPM observation. Spherical carbides on the matrix are observed by a SEM as white spotty parts (Fig. 12 (a)). In addition, some spherical carbide particles were observed on a surface of the specimen from the birds-eye pattern shown in Fig. 12 (c).

The sizes of a carbide particle in the specimen and convex particle in the GBF area were measured by a computer-aided image processor based on an SPM-image. The results in Fig. 13 relate the area of the particles to the

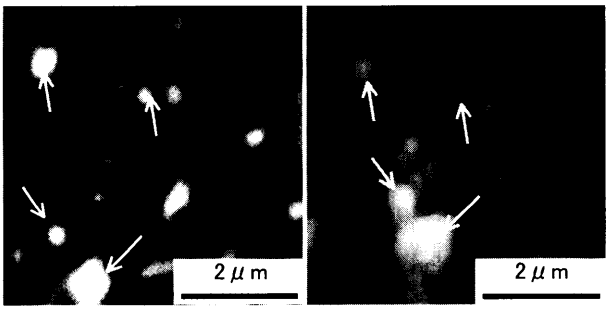

(a) SEM micrograph showing the area observed by SPM (b) SPM image of the GBF area

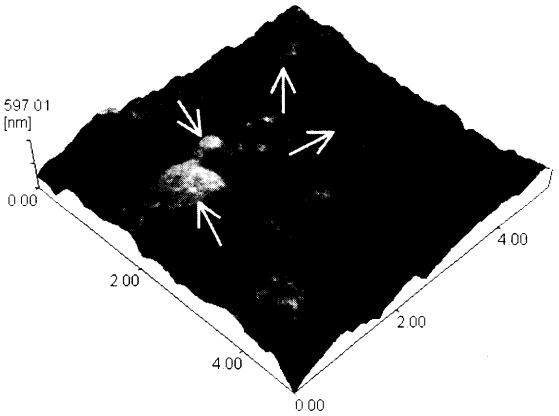

(c) Birds-eye pattern of the GBF area in (b)

Fig. 11 Detailed observation of the GBF area on the fracture surface of the Type A specimen by SPM; (a) SEM micrograph showing the area observed by SPM, (b) SPM image and (c) Birds-eye pattern of the GBF area in (b)

number of particles. Sizes and distribution of convex particles in the GBF area correspond to those of carbide ones in the microstructure of the tested materials. The average area of a convex particle in the GBF area was 0.68 μm^2 (diameter 1.10 μm), equivalent to an average area of a carbide particle of 0.72 μm^2 (diameter 1.13 μm). These values are also equivalent to an average distance of roughness, S, (Table 1). Therefore, it is considered from these experimental results that the formation of rough and granular surface relates to the carbide particles in the microstructure of the specimens.

5.2 Carbon distribution in GBF area by EPMA

Assuming some roughness is formed on the fracture surface in the GBF area by the remaining carbide particles and the marks of those peeled off, a high density of carbon should be detected on the GBF area. Figures 14 and 15 show the distribution of carbon, molybdenum and tungsten near a non-metallic inclusion on the fracture surface of Type A and Type B specimens by Electron Probe Microanalysis (EPMA). It can be seen from Fig. 14 that rich carbon distribution is detected in the GBF area of the Type A specimen compared with outside the GBF. On the

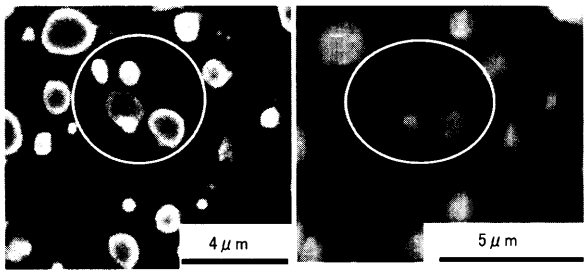

(a) SEM micrograph showing the area observed by SPM (b) SPM image of microstructure

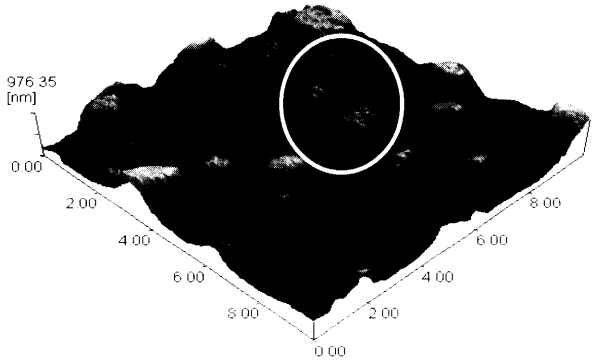

(c) Birds-eye pattern of the area in (b)

Fig. 12 Detailed SPM observation of the microstructure of the tested materials; (a) SEM micrograph showing the area observed by SPM, (b) SPM image and (c) Birds-eye pattern of the area in (b)

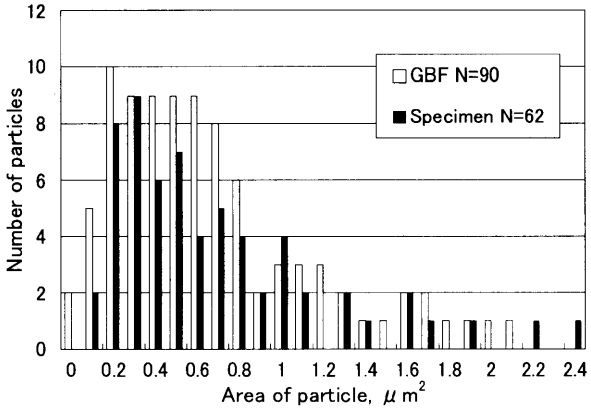

Fig. 13 Experimental measurements for size distribution of the convex particles in the GBF area observed by SPM and the carbide particles in the microstructure of the tested materials

other hand, carbons on the fracture surface of the Type B specimen are distributed uniformly near an inclusion, and the density of carbon is lower than in the GBF area in the Type A specimen as shown in Fig. 15. The difference in the density of molybdenum and tungsten cannot be observed between both specimens. It is concluded from these experimental results that carbide particles in a specimen come into existence on the fracture surface around an inclusion during the fracture process.

5.3 GBF formation model

The experimental results obtained from the high speed tool steel, JIS SKH51, were almost same as a high-carbon-chromium bearing steel, JIS SUJ2, which contains 1.01%w/w carbon as reported previously[19),(20)]. Based on the experimental results, a mechanism for the formation of the GBF area during the high-cycle fatigue process is proposed as a 'dispersive decohesion of spherical carbide' model, which was proposed for a high-carbon-chromium bearing steel in previous papers[19),(20)]. The model is illustrated in Fig. 16.

Initially, multiple microcracks are dispersed by decohesion of spherical carbide from the matrix near a non-metallic inclusion (see Fig. 16 (a)). These microcracks grow and coalesce with each other during fatigue cycles (Fig. 16 (b)). At this time, the microcracks propagate along a boundary between the spherical carbide and matrix, and therefore the roughness of the size of the carbide grade is generated on the fracture surface. The propagation of microcracks may be very slow at this time, and a GBF area forms. After formation of an appropriate size for the GBF area to enable propagation as an ordinary crack, the crack propagates without depending on the microstructure of the materials and forms a fish-eye, as shown in Fig. 16 (c). As a result, a greater roughness of the fracture surface in the GBF area (compared with the surrounding area) is formed by the carbide particles that remain and holes from which others have been peeled off from the matrix. The roughness outside the GBF area is small because the crack propagates in the matrix as shown in Fig. 16 (d). It was suggested from the detailed observations shown in Figs. 6 and 7 that fine spherical carbides such as chromium carbides and iron carbides (cementite, Fe_3C) peel off from the matrix, and large carbide particles combined with molybdenum, vanadium and tungsten are ruptured during the GBF formation process with cycling as illustrated in Fig. 16 (c). It is considered that the rea-

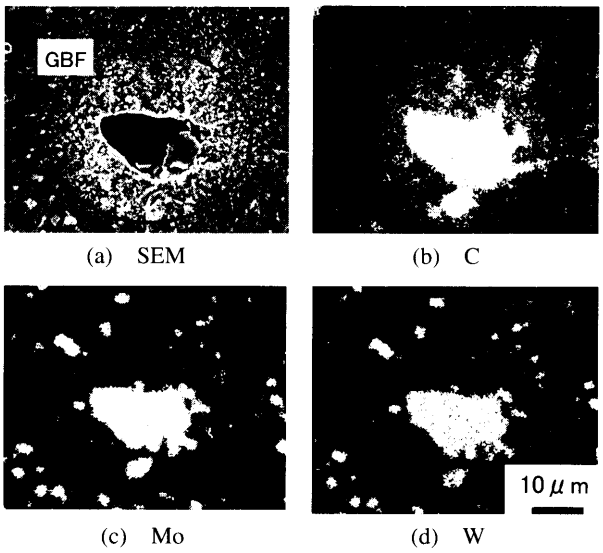

Fig. 14 Distributions of C, Mo and W around an inclusion of a Type A specimen by EPMA

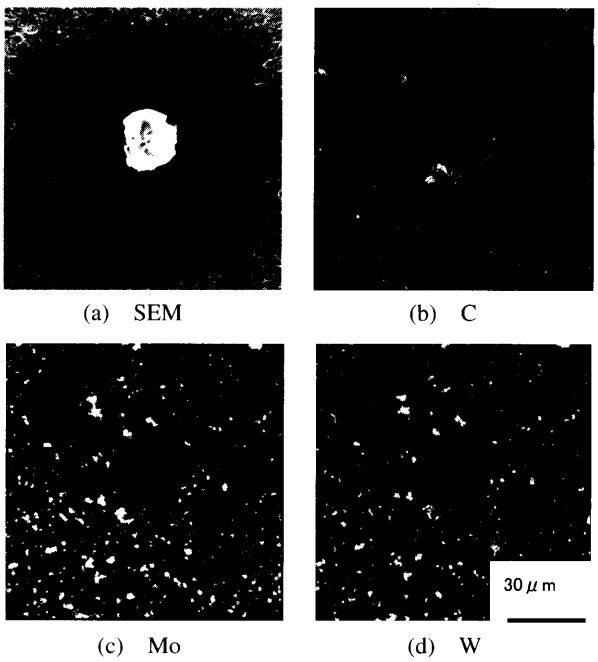

Fig. 15 Distributions of C, Mo and W around an inclusion of a Type B specimen by EPMA

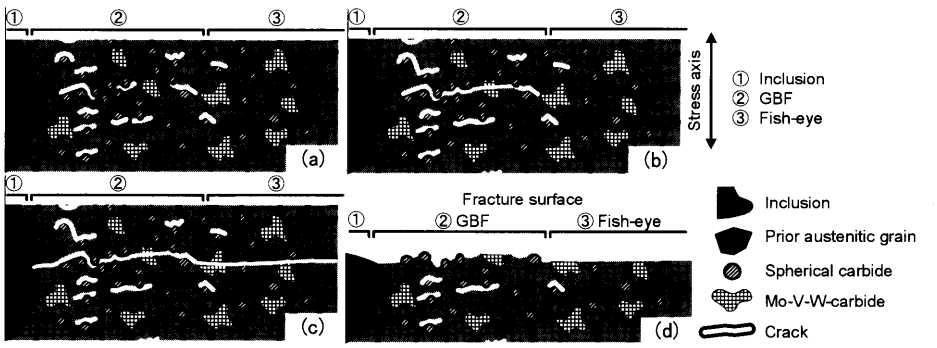

Fig. 16 Proposed model, 'dispersive decohesion of spherical carbide', for the formation of the GBF area around an inclusion during a super-long fatigue process

son why the fracture behavior is different between kinds of carbides originates from the ability to adhere and deform between the carbide and the matrix.

As noted in previous paper[16),(22)], the GBF area is generated in an early stage of the fatigue cycles, at about 10% of fatigue life, and a large percentage of the fatigue life is spent forming a suitable GBF area size, which can be described by dispersive generation, slow growth and the coalescence of microcracks in the vicinity of an inclusion during the fatigue process. The formation of a GBF area near a non-metallic inclusion is required for a fatigue fracture in a very high cycle fatigue regime, since the stress intensity factor around an inclusion is below the threshold value for crack initiation and propagation. On the other hand, a fatigue crack occurs at an inclusion due to the stress concentration without the formation of a GBF area, under high-stress amplitude levels and a low number of cycles.

6. Conclusions

To clarify the mechanisms of subsurface crack initiation and propagation for a high-strength steel in very high cycle fatigue regime, detailed observations and analysis of a fracture surface by a three-dimensional SEM and SPM, and computational simulation of the fracture process by FRASTA were conducted. Specimens of a high speed tool steel, JIS SKH51, obtained from a cantilever-type rotary bending fatigue in air were assessed.

Conclusions obtained in this study are as follows:

(1) The roughness in a distinctive feature of the fracture surface, named a granular-bright facet (GBF), was very large compared with the surface outside the GBF, and of similar size to the fine spherical carbide particles in the microstructure of the tested materials. In addition, the size and distribution of convex particles in the GBF area corresponds to those of carbide particles in the microstructure of the tested materials.

(2) Rich carbon distribution in the GBF area, compared with that outside the GBF, was detected by EPMA.

(3) From the above two experimental conclusions, it was inferred that the formation of the rough and granular fracture surfaces in the GBF area relate to fine carbide particles in the microstructure.

(4) From the computational simulation using the FRASTA method, multiple microcracks are dispersed in the vicinity of an inclusion, grow, and then coalesce with each other under a very high cycle fatigue regime. On the other hand, a fatigue cracks occur at an inclusion and grows continuously under conditions of a high-stress amplitude level and a low number of cycles.

(5) The mechanism of GBF formation in a very high cycle fatigue regime was proposed as the 'dispersive decohesion of spherical carbide' model. This model was confirmed to come into existence for steel that contains different carbon percentages.

Acknowledgments

This work was supported by Grant-in Aid for Scientific Research (C), No.15560065, Japan Society for the Promotion Science.

References

(1) Ochi, Y. and Sakai, T., Fundamentals and Recent Topics on Fatigue III: Fatigue of Metallic Materials in the Very High Cycle Regime, J. Soc. Mat. Sci. Jpn., (in Japanese), Vol.52, No.4 (2003), pp.433–439.

(2) Shiozawa, K., Characteristics of Fatigue Behavior of Surface Modified Materials, Macro and Microscopic Approach to Fracture, Edited by Nishida, S.-I., (2003), pp.117–170, WIT Press.

(3) Murakami, Y., Takada, M. and Toriyama, T., Super-Long Life Tension-Compression Fatigue Properties of Quenched and Tempered 0.46% Carbon Steel, Int. J. Fatigue, Vol.20, No.9 (1998), pp.661–667.

(4) Shiozawa, K., Lu, L. and Ishihara, S., $S-N$ Curve Characteristics and Subsurface Crack Initiation Behaviour in Ultra-Long Life Fatigue of a High Carbon-Chromium Bearing Steel, Fatigue Fract. Engng. Mater. Struct., Vol.24, No.12 (2001), pp.781–790.

(5) Wang, Q.Y., Berard, Y., Dubarre, A., Baudry, G., Rathery, S. and Bathias, C., Gigacycle Fatigue of Ferrous Alloys, Fatigue Fract. Engng. Mater. Struct., Vol.22, No.7 (1999), pp.667–672.

(6) Nishijima, S. and Kanazawa, K., Stepwise $S-N$ Curve and Fish-Eye Failure in Gigacycle Fatigue, Fatigue Fract. Engng. Mater. Struct., Vol.22, No.7 (1999), pp.601–607.

(7) Murakami, Y., Nomoto, T. and Ueda, T., Factors Influencing the Mechanism of Superlong Fatigue Failure in Steels, Fatigue Fract. Engng. Mater. Struct., Vol.22, No.7 (1999), pp.581–590.

(8) Nakajima, M., Sakai, T. and Shimizu, T., An Observation of Fish-Eye Fracture Process in High Strength Steel SUJ2, Trans. Jpn. Soc. Mech. Eng., (in Japanese), Vol.65, No.640, A (1999), pp.2504–2510.

(9) Sakai, T., Takeda, M., Shiozawa, K., Ochi, Y., Nakajima, M., Nakamura, T. and Oguma, N., Experimental Evidence of Duplex $S-N$ Characteristics in Wide Life Region for High Strength Steels, Fatigue '99: Proc. of the Seventh Inter. Fatigue Cong., Edited by Wu, X.R. and Wang, Z.G., Vol.1 (1999), pp.573–578, Higher Edu Press.

(10) Sakai, T., Takeda, M., Shiozawa, K., Ochi, Y., Nakajima, M., Nakamura, T. and Oguma, N., Experimental Reconfirmation of Characteristic $S-N$ Property for High Carbon Chromium Bearing Steel in Wide Life Region in Rotating Bending, J. Soc. Mater. Sci. Jpn., (in Japanese), Vol.49, No.7 (2000), pp.779–785.

(11) Sakai, T., Takeda, M., Tanaka, N., Kanemitsu, M., Oguma, N. and Shiozawa, K., Characteristic $S-N$ Property of High Carbon Chromium Bearing Steel in Ultra-Wide Life Region under Rotating Bending, Mat. Sci. Res. Int., STP-1, (2001), pp.41–46, Soc. Mat. Sci. Jpn.

(12) Murakami, Y., Nomoto, T., Ueda, T., Murakami, Y. and Ohbori, M., Analysis of the Mechanism of Superlong Fatigue Failure by Optical Microscope and SEM/AFM Observations, J. Soc. Mater. Sci. Jpn., (in Japanese), Vol.48, No.10 (1999), pp.1112–1117.

(13) Murakami, Y., Yokoyama, N.N. and Takai, K., Effect of Hydrogen Trapped by Inclusions on Ultra-Long Life Fatigue Failure of Bearing Steel, J. Soc. Mat. Sci. Jpn., (in Japanese), Vol.50, No.10 (2001), pp.1068–1073.

(14) Ochi, Y., Matsumura, T., Masaki, K. and Yoshida, S., High-Cycle Rotating Bending Fatigue Property in Very Long-Life Regime of High-Strength Steels, Fatigue Fract. Engng. Mater. Struct., Vol.25, No.8/9 (2002), pp.823–830.

(15) Shiozawa, K. and Lu, L., Very High-Cycle Fatigue Behaviour of Shot-Peened High-Carbon-Chromium Bearing Steel, Fatigue Fract. Engng. Mater. Struct., Vol.25, No.8/9 (2002), pp.813–822.

(16) Lu, L. and Shiozawa, K., Effect of Two-Step Load Variation on Gigacycle Fatigue and Internal Crack Growth Behavior of High Carbon-Chromium Bearing Steel, VHCF-3: Proc. of the Third Inter. Conf. on Very High Cycle Fatigue, Edited by Sakai, T. and Ochi, Y., (2004), pp.185–192, Soc. Mater. Sci. Jpn.

(17) Lu, L., Shiozawa, K. and Morii, Y., Gigacycle Fatigue Behavior and Fracture Morphology of High Speed Tool Steel, JIS SKH51, Trans. Jpn. Soc. Mech. Eng., (in Japanese), Vol.69, No.679, A (2003), pp.662–670.

(18) Lu, L. and Shiozawa, K., Effect of Surface Treatment on Super-Long-Life Fatigue Behavior in High Speed Tool Steel, JIS SKH51, Trans. Jpn. Soc. Mech. Eng., (in Japanese), Vol.69, No.684, A (2003), pp.1195–1202.

(19) Shiozawa, K., Morii, Y., Nishino, S. and Lu, L., A Study of Subsurface Crack Initiation and Propagation Mechanism of High-Strength Steel by Fracture Surface Topographic Analysis, J. Soc. Mat. Sci. Jpn., (in Japanese), Vol.52, No.11 (2003), pp.1311–1317.

(20) Shiozawa, K., Nishino, S. and Morii, Y., Subsurface Crack Initiation and Propagation Mechanism of High-Strength Steel in Very High Cycle Fatigue Regime, VHCF-3; Proc. of the Third Inter. Conf. on Very High Cycle Fatigue, Edited by Sakai, T. and Ochi, Y., (2004), pp.85–92, Soc. Mat. Sci. Jpn.

(21) Kobayashi, T. and Shockey, D.A., FRASTA: A New Way to Analyze Fracture Surfaces, Ad. Mater. & Processes, Vol.140, No.5 (1991), pp.28–34.

(22) Lu, L. and Shiozawa, K., Effect of Two-Step Load Variation on Super-Long Life Fatigue and Internal Crack Growth Behavior of High Carbon-Chromium Bearing Steel, Trans. Jpn. Soc. Mech. Eng., (in Japanese), Vol.68, No.675, A (2002), pp.1666–1673.